



X-ray phase contrast simulation for grating-based interferometry using GATE

JONATHAN SANCTORUM,*  JAN DE BEENHOUWER, AND JAN SIJBERS

imec-Vision Lab, Dept. of Physics, University of Antwerp, Universiteitsplein 1, 2610 Antwerpen, Belgium
**jonathan.sanctorum@uantwerpen.be*

Abstract: The overall importance of x-ray phase contrast (XPC) imaging has grown substantially in the last decades, in particular with the recent advent of compact lab-based XPC systems. For optimizing the experimental XPC setup, as well as benchmarking and testing new acquisition and reconstruction techniques, Monte Carlo (MC) simulations are a valuable tool. GATE, an open source application layer on top of the Geant4 simulation software, is a versatile MC tool primarily intended for various types of medical imaging simulations. To our knowledge, however, there is no GATE-based academic simulation software available for XPC imaging. In this paper, we extend the GATE framework with new physics-based tools for accurate XPC simulations. Our approach combines Monte Carlo simulations in GATE for modelling the x-ray interactions in the sample with subsequent numerical wave propagation, starting from the GATE output.

© 2020 Optical Society of America under the terms of the [OSA Open Access Publishing Agreement](#)

1. Introduction

X-ray phase contrast (XPC) computed tomography (CT) is well known for its ability to generate contrasts that are complementary to conventional absorption contrast (AC). The introduction of compact lab-based systems for phase sensitive imaging has boosted research in XPC in the past decade, and a multitude of applications has risen, covering a broad field ranging from (bio)medical imaging (e.g., soft tissue) to materials science (e.g., low-density materials) [1]. Fibrous or porous materials, found in biological tissue (e.g., dentinal tubules in teeth) and advanced composite materials (e.g., fiber reinforced polymers) are often of particular interest, in order to relate the inner microstructure to their macroscopic properties. By exploiting the so-called dark field contrast (DFC) [2], information about the microstructure can be revealed even when the structures are not resolvable by the detector. DFC, which is attributed to small-angle scattering in the sample, is closely related to phase contrast and both can be measured in a single experiment with, for example, a grating-based interferometer (GBI) [3]. The imaging principle of such interferometers is based on the Talbot effect and GBIs are a valuable tool for acquiring PC images with conventional sources [4]. In practice, a GBI does not directly measure the phase but its first derivative, and the generated contrast is therefore referred to as differential phase contrast (DPC). In addition to the DPC and DFC images, this method also yields the conventional AC image.

When investigating new CT acquisition and reconstruction procedures, computational x-ray simulations are a valuable tool for benchmarking and testing. GATE [5], an open source application layer on top of the Geant4 [6] simulation software, is a versatile Monte Carlo (MC) tool for various types of medical imaging simulations, including CT [7]. Unfortunately, tools for XPC imaging are currently not available within GATE.

As for XPC simulations, a number of different approaches have been proposed, based on either numerical wave propagation [8,9], MC simulations [10,11], or a combination of both [12,13]. More recently, the combination of analytical and empirical input data has been explored to reduce simulation times [14]. The latter approach, however, does not include dark field imaging.

Therefore, we propose a combination of Monte Carlo simulations in GATE for modelling the x-ray interactions in the sample, and subsequent numerical wave propagation, towards the detection plane. This paper builds upon earlier work by Peter et al. [13], where this combination is employed. To this end, we extend the existing GATE framework with additional tools for the purpose of XPC simulations. We review the principles of grating-based XPC CT and discuss the simulation framework. Finally, we show and discuss the simulation results.

2. Methods

In this section, we will first briefly address the imaging principles underlying grating-based interferometry in Section 2.1, as well as the general GATE framework (Section 2.2), followed by a discussion concerning the simulation approach and the corresponding additions to GATE. The concept of using a consecutive combination of MC simulation and wavefront propagation for XPC was originally introduced by Peter et al. [13], where `egs++` was chosen as MC framework. In this paper, we will pave the way for the simulation of advanced contrast modalities using GATE's versatile macro interface. Moreover, we will address aspects that were unexplored in their work, e.g. 2D radiography including advanced phantom design (Section 3). Different approaches to the wavefront construction will be presented, as well as a thorough investigation of the implementation of phase stepping and phase retrieval.

2.1. Principles of grating-based interferometry

A grating-based interferometer relies on a coherent x-ray source that emits x-rays towards a detector. On their path to the detector, the x-rays encounter two gratings: G_1 and G_2 [15], as shown in Fig. 1. Synchrotron facilities meet the requirement of coherence, but lab sources do not. This can, however, be overcome by introducing a third grating (G_0 , not shown) before the first one (G_1), as will be discussed further in this section. The first grating (G_1) in Fig. 1 generates an interference pattern at regular distances with the same period as that of grating G_1 , or a fraction thereof. This pattern is known as the Talbot carpet and the distances d_n at which it occurs are accordingly known as (fractional) Talbot distances [16,17]:

$$d_n = n \frac{1}{\eta^2} \frac{g_1^2}{2\lambda}, \quad (1)$$

where n is an integer called the Talbot order, λ is the wavelength of the radiation and g_1 is the pitch of the first grating G_1 . If G_1 is an amplitude grating or a $\pi/2$ -shifting phase grating, then $\eta = 1$; if G_1 is a π -shifting phase grating, $\eta = 2$. Amplitude gratings will exhibit maximum fringe contrast at even Talbot orders, while phase gratings do so at odd Talbot orders.

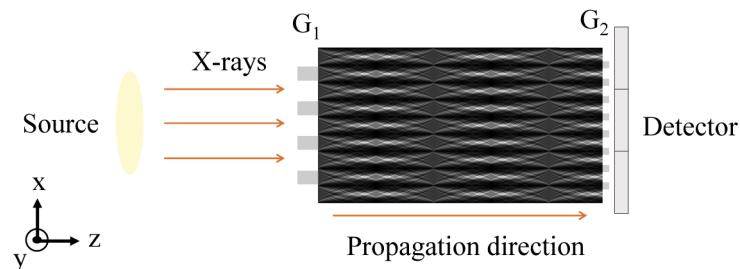


Fig. 1. Schematic overview of a grating-based interferometer (not to scale).

As mentioned earlier, it can be shown [18] that by inserting an additional absorption grating (G_0) in front of the x-ray source, a sufficiently strong interference pattern can be generated, even

if incoherent sources are used for imaging [4]. The slits of the source grating will act as an array of mutually incoherent sources, which, due to their reduced individual widths are each in itself small enough to be sufficiently spatially coherent. By carefully scaling the distances between the three gratings, the interference patterns caused by the individual slits will coincide at a specific Talbot distance. The coinciding patterns all incoherently contribute to a single detectable pattern. For the sake of simplicity, we will assume in the following that the source already is coherent.

Placing an object in the beam will distort the wavefront, causing the interference pattern to change. As the fringes of the interference pattern are not resolvable by the detector, these changes cannot be measured directly. Therefore, an absorbing analyser grating (G_2) is placed directly in front of the detector, which has a pitch that matches the periodicity of the undistorted interference pattern at that position. By shifting this grating along x (Fig. 1), the portion of the interference pattern intensity that is being transmitted varies. This generates for every detector pixel an intensity curve that oscillates as a function of the x -translation of G_2 , hereby effectively translating the undetectable phase modulation into a detectable intensity modulation. The parameters defining these curves can be retrieved from a set of images taken at different G_2 positions x_g , a procedure known as phase stepping, using a phase retrieval algorithm [19].

In the ideal case, the modulation of the intensity can be modeled by a triangle wave [20]. The triangular wave function f_{TW} is given by

$$f_{\text{TW}} = \frac{2}{\pi} \arcsin(\sin x), \quad (2)$$

and the ideal case model is written as

$$I(i, j, x_g) = a_0(i, j) + a_1(i, j) f_{\text{TW}} \left[2\pi \frac{x_g}{g_2} + \phi_1(i, j) + \pi \right], \quad (3)$$

where g_2 denotes the pitch of the analyser grating G_2 . The phase factor $+\pi$ is introduced to match the interpretation of ϕ_1 in Eq. (3) to the interpretation in Eq. (4), as the latter is more common in literature.

Due to system imperfections such as variations in the widths and periodicity of the gratings, detector imperfections, polychromaticity, and mainly the incoherence of the source, the intensity will be blurred in real-life measurements [20] (Fig. 2). Therefore, the phase stepping curve corresponding to detector pixel (i, j) is typically described by a cosine function [3,21]:

$$I(i, j, x_g) = a_0(i, j) + a_1(i, j) \cos \left[2\pi \frac{x_g}{g_2} + \phi_1(i, j) \right]. \quad (4)$$

By estimating the model parameters a_0 , a_1 , and ϕ_1 from the intensity modulation curve with object in the beam ($I_s(i, j, x_g)$) as well as from the intensity modulation curve without object in the beam ($I_r(i, j, x_g)$), the AC (T), DPC ($\nabla_x \Phi$) and DFC (V) images can be calculated in every pixel [3]:

$$T(i, j) = \frac{a_{0,s}(i, j)}{a_{0,r}(i, j)}, \quad (5)$$

$$\nabla_x \Phi(i, j) = \frac{g_2}{\lambda d} [\phi_{1,s}(i, j) - \phi_{1,r}(i, j)], \quad (6)$$

$$V(i, j) = \frac{a_{1,s}(i, j)/a_{0,s}(i, j)}{a_{1,r}(i, j)/a_{0,r}(i, j)}, \quad (7)$$

with d the distance between G_1 and G_2 . The AC signal is hence the constant offset of the phase stepping curve, while the first derivative of the phase of the wavefront is related to the phase shift of the intensity modulation curve compared to the reference curve. The DFC signal is determined

by the relative amplitude of the curve, which can be understood as a measure of how visible the interference pattern is. Increased scattering will result in increased blurring of the interference pattern, thereby reducing the stepping curve's amplitude, which is why the DFC signal is often referred to as the "visibility".

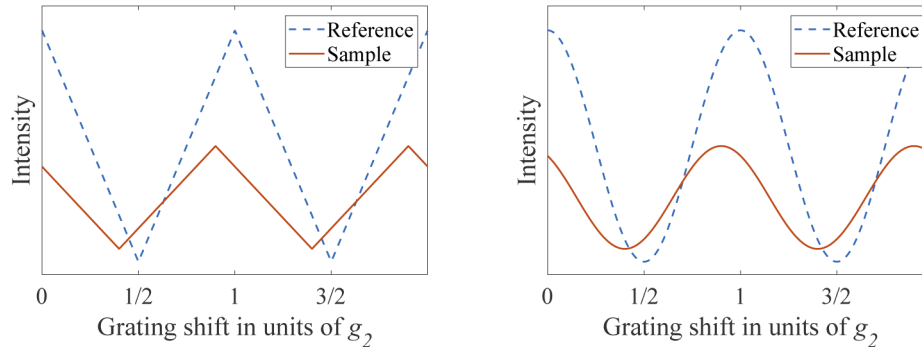


Fig. 2. (left): Ideal case triangular phase stepping curves. (right): Cosine shaped phase stepping curves.

The phase retrieval, which is the estimation of the function parameters from the phase stepping measurements, can be performed through different procedures. In real measurements, the parameters can be estimated from a least squares fit of a sine (or cosine) to the measured points [20]. Alternatively, Eq. (4) can be treated as the first order approximation of a Fourier series [3].

In order to interpret the simulation results without the influence of detector effects, the simulations are performed without realistic detector modelling. Without loss of generality, we will continue with the ideal case imaging conditions, and therefore Eq. (3) is used for fitting whenever phase retrieval is performed. In Appendix A, a practical method is presented for automated fitting of Eq. (3) to phase stepping data.

2.2. GATE

GATE is a MC platform developed since 2001 by the OpenGATE collaboration and was first publicly released in 2004. Initially, the main goal of the platform was the modelling of planar scintigraphy, single photon emission computed tomography (SPECT), and positron emission tomography (PET) acquisitions [5]. The features of the platform have been enhanced over the years, resulting in regular releases of new versions of the software. In this way, GATE stays consistent with regular Geant4 public releases while being upgraded. The GATE architecture consists of a Geant4 kernel surrounded by three specific layers. Firstly, the core layer defines the basic simulation elements such as geometry, source, and physical processes. The next layer is the application layer, using the basic elements of the core layer, to model objects and processes specific to the imaging applications. Finally, GATE has a user layer, providing a scripting environment to set up a simulation without any C++ coding. Despite regular advances in the list of GATE functionalities, for example with respect to CT [7], XPC has not been taken into account apart from our preliminary work [22].

2.3. Extension of the GATE source code

GATE forms the first part of the simulation pipeline, where the x-ray interactions in the phantom are simulated (Section 2.3.1). After these interactions, the x-rays are collected in a discretized wavefront at a virtual plane behind the phantom (Section 2.3.3). These modifications were implemented in GATE version 8.0. In the second part of the simulation, the constructed wavefront

interacts with the gratings and is propagated towards the detector (Section 2.4.1). Here, phase stepping is performed. A schematic overview of the simulation flow is shown in Fig. 3.

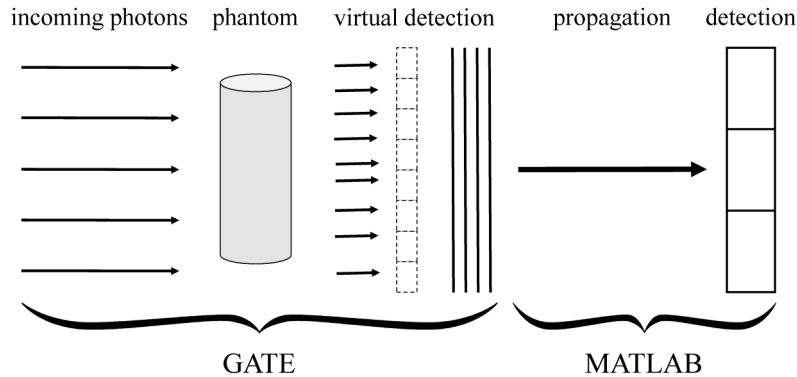


Fig. 3. Schematic overview of the implemented simulation framework.

2.3.1. Introducing phase effects in GATE

As mentioned in the introductory section, the physics related to the absorption effects is already present in GATE. However, as described in [13], taking phase effects into account requires the photons to have an additional property (a phase or optical path) and the inclusion of an additional physics process. In order to define these, each material in the simulation is associated with its complex index of refraction, $n = 1 - \delta + i\beta$, more specifically the decrement of its real part, δ . This was implemented in such a way that the user can easily add this property to the GATE material database on request by specifying a set of δ -values in the macro (a GATE script configuring a simulation) for a custom energy range:

```
/gate/refractiveindex/setRefractiveIndex 'name' 'E1' 'd1'
/gate/refractiveindex/setRefractiveIndex 'name' 'E2' 'd2'
...
```

The material name is denoted by 'name'. Next, the energy and δ values are specified. These values can be extracted from data tables [23], or directly from http://henke.lbl.gov/optical_constants/. Having defined the material properties for PC, a phase ϕ is associated with each photon p . When travelling through a certain material, the phase added to the photon's original phase is given by:

$$\phi = k_p \int \delta(\mathbf{r}) ds, \quad (8)$$

where k_p is the photon's wave number in vacuum and the integral is calculated over the path followed by the photon. Tracking of the optical path length was done using the processGate library [24]. Furthermore, the physics library of GATE was extended with an x-ray refraction process. At the boundary between one material (with refractive index decrement δ_1) and another (with refractive index decrement δ_2), the photon undergoes a deterministic refraction process, governed by Snell's law [10]

$$(1 - \delta_1) \sin \theta_1 = (1 - \delta_2) \sin \theta_2. \quad (9)$$

with θ_1 the angle between the direction of the incoming photon in the first material and the surface normal, and θ_2 the angle between the direction of refracted photon in the second material

and the surface normal. The refraction process (named XrayRefraction) was implemented in the GATE source code, and can be activated in the macro, similar to other physics processes:

```
gate/physics/addProcess XrayRefraction
```

2.3.2. Introducing surface roughness

Since refraction is included in our GATE simulations, the roughness of the surface at which it occurs must be considered. To this end, we propose to use a simplified but effective model. For the refraction process, the key aspect of surface roughness in refraction processes, is the local orientation of the surface normal. Hence, the roughness modelling can be simplified, by introducing local variations in the surface normal with respect to the mean surface, using a stochastic model. The local surface normal undergoes a slight deflection from its original position every time a photon hits, and the direction for the deflection is drawn uniformly from the full 4π solid angle. The magnitude follows a Gaussian distribution, expressing the expectation that smaller deviations are more likely than larger ones. Other probability distributions could be of interest depending on e.g. the designed phantom, but such a discussion exceeds the scope of our work. This surface roughness model was applied to the simulations described in Section 3.2 and Section 3.3. We note that our approach to model the surface roughness is similar to the already present treatment of optical photons in GATE for e.g. explicit modelling of scintillator effects.

2.3.3. Wave front construction in GATE

After interacting with the phantom, the photons arrive at a virtual plane, positioned directly behind the phantom. To compute the actual X-ray wavefront in that plane, the photons are coherently added, based on their position, energy, and phase. In GATE, this is achieved by defining a physical detector plane directly behind the phantom, which acts as a virtual intermediate detector. This plane is not the actual detector in the simulation, but only serves to switch from a particle representation to a wave representation. Subsequently, for each photon, the position where it first hits the virtual detector plane is determined, and this position is used to assign the photon to a certain wavefront pixel. In this way, the wavefront is generated in GATE, one photon at a time. Rather than adding intensities, as one would do for standard absorption imaging, complex amplitudes are added. In this way, interference effects are accounted for in the final part of the simulation, where the wave propagation and the interaction with the gratings is implemented (Section 2.4.1).

In GATE, the wavefront construction is done by discretizing the two-dimensional virtual plane into $N_x \times N_y$ pixels of size $\Delta x \times \Delta y$. To coherently add the photons arriving at the same pixel, the photons are assigned complex wave amplitudes Ψ . Given that every photon p represents a position in the plane \mathbf{r} , an energy E , and a phase ϕ , we write $p \rightarrow p\{\mathbf{r}, E, \phi\}$. Using this notation, we transform the particle representation to a wave representation at position \mathbf{r} :

$$p\{\mathbf{r}, E, \phi\} \iff p\{\mathbf{r}, \Psi(E, \phi)\}, \quad (10)$$

where

$$\Psi(E, \phi) = \sqrt{E} \exp(-i\phi). \quad (11)$$

The position \mathbf{r} determines to which pixel of the wavefront a certain photon contributes. If we write $\mathbf{r} = (r_x, r_y)$ and define the continuous coordinates of the central point of pixel (x, y) as (x_c, y_c) , the condition for arriving at a certain pixel is given by

$$\begin{aligned} p\{\mathbf{r}, \Psi(E, \phi)\} &\in P(x, y) \\ &\iff \left(r_x \in [x_c - \Delta x/2, x_c + \Delta x/2[\right) \wedge \left(r_y \in [y_c - \Delta y/2, y_c + \Delta y/2[\right), \end{aligned} \quad (12)$$

where $P(x, y)$ is the set of photons arriving at wavefront pixel (x, y) .

Assuming $N(x, y)$ photons arrive in pixel (x, y) and using the photons' wave representations, the coherent addition of the complex amplitudes Ψ_n is written as:

$$D(x, y) = \sum_{n=1}^{N(x,y)} \Psi_n = \sum_{n=1}^{N(x,y)} \sqrt{E_n} \exp(-i\phi_n). \quad (13)$$

In Eq. (13), $D(x, y)$ denotes the complex wavefront amplitude resulting from the contributions of the $N(x, y)$ photons arriving at pixel (x, y) . By adding complex wave amplitudes rather than only phases, both the gained phase and the photon energy of each photon are taken into account when determining the contributions to the total complex amplitude of the wavefront. The employed complex amplitude summation allows to simulate interference effects at the point of transition to a wavefront, in order to construct the correct initial state of the wavefront. The sum is formulated as:

$$D(x, y) = \sum_{n=1}^{N(x,y)} \sqrt{E_n} \cos \phi_n - i \sum_{n=1}^{N(x,y)} \sqrt{E_n} \sin \phi_n. \quad (14)$$

In our implementation, the real and imaginary part of the wavefront is stored in two data vectors, rather than its energy and phase. However, both representations are completely equivalent.

The user defines the number of pixels in the gridded plane with the following macro commands

```
/gate/processGate/setGridX 'number of pixels'
/gate/processGate/setGridY 'number of pixels'
```

The corresponding dimensions are defined using

```
/gate/processGate/setPhysicalGridX 'size'
/gate/processGate/setPhysicalGridY 'size'
```

However, deciding on the grid spacing requires careful thought. Indeed, taking the numerical wavefront propagation described in Section 2.4.1 into account, the pixel size of the wavefront must allow sampling the smallest structures in the simulation [9].

In total, three such grids are generated as output: the real part, the imaginary part and the number of arriving photons:

```
/gate/processGate/setOutputNameReal 'filename'
/gate/processGate/setOutputNameImag 'filename'
/gate/processGate/setOutputNameCounts 'filename'
```

The wavefront construction is initialised in the macro using

```
/gate/processGate/enableGrid
```

As was the case for the XrayRefraction process, the wavefront construction relies on the processGate library for the collection of photons at the virtual plane.

2.4. Processing GATE output

In the second part of the simulation, the resulting wavefront from GATE interacts with grating G_1 and is further propagated towards G_2 (Section 2.4.1). After interacting with G_2 , the detection takes place and phase stepping is performed.

2.4.1. Wavefront propagation

The GBI system is modelled as a sequence of three events. The first event is the interaction of the wavefront with the first grating G_1 , which we will assume to be a phase grating. This interaction introduces a phase modulation in the wavefront. Subsequently, the resulting wavefront propagates through free space (second event) towards the absorption grating G_2 and the detector, which form the final part of the imaging system. In our work, this three-step imaging protocol was implemented in MATLAB. Hence, the binary files containing the real and imaginary vectors of the wavefront are first loaded in MATLAB and reshaped to the original size of the wavefront.

An ideal G_1 phase grating is constructed by using a superposition of two identical rectangular Dirac combs, of which one is shifted along the x -direction by the grating bar width and multiplied by an exponential phase factor $\exp(i\phi)$ [25]. This yields a grating that has 100% transmission over its full range, but introduces a phase shift of ϕ in a regular pattern. For Talbot-interferometry, this phase shift is either π or $\pi/2$. Mathematically, a phase grating with bar width b and pitch g_1 is expressed as

$$G_1(x) = \text{comb}\left(\frac{x}{g_1}\right) * \left(\left[\text{rect}\left(\frac{x}{b}\right) * \delta(x) \right] + \left[\text{rect}\left(\frac{x}{b}\right) * \delta(x-b) \right] \exp(i\phi) \right), \quad (15)$$

where $*$ denotes the convolution operator, the comb function can be written as

$$\text{comb}\left(\frac{x}{g_1}\right) = \sum_{n=-\infty}^{+\infty} \delta(x - ng_1), \quad (16)$$

and

$$\text{rect}\left(\frac{x}{b}\right) = \begin{cases} 1, & x \in \left[-\frac{b}{2}, \frac{b}{2}\right] \\ 0, & \text{otherwise} \end{cases}. \quad (17)$$

The effect of G_1 on the wavefront is subsequently simulated through a pointwise multiplication of the wavefront with the 2D extension of the $G_1(x)$ function. Straightforward implementation is achieved through the built-in MATLAB function *pulstran*. Propagation of a wavefront is described with the Huygens-Fresnel principle [26]. Assuming the Fresnel-approximation holds, the propagation of the wavefront is described using a propagator kernel h as follows:

$$D(x_1, y_1, z) = \int_{-\infty}^{+\infty} \int_{-\infty}^{+\infty} D(x, y, 0) h(x_1 - x, y_1 - y) dx dy. \quad (18)$$

Eq. (18) yields the complex amplitude $D(x_1, y_1, z)$ of the wavefront at position (x_1, y_1) after propagating a distance z . The convolution kernel is given by

$$h(x, y) = \frac{\exp(ikz)}{i\lambda z} \exp\left[\frac{ik}{2z}(x^2 + y^2)\right]. \quad (19)$$

For numerical applications, Eq. (18) cannot be used directly and requires discretization, which involves sampling of the convolution kernel. Assuming sampling is performed in Fourier space, we introduce the discrete formulation of the propagation [27]:

$$D(x, y, z) = \exp(ikz) \text{DFT}^{-1} \left(\exp\left[\frac{-iz(k_x^2 + k_y^2)}{2k}\right] \text{DFT}[D(x, y, 0)] \right), \quad (20)$$

where DFT denotes the discrete Fourier transform and k_x and k_y are discrete sampling positions in Fourier space, with grid spacings Δk_x and Δk_y . The latter are given by

$$\Delta k_x = \frac{2\pi}{N_x \Delta x}, \quad (21)$$

$$\Delta k_y = \frac{2\pi}{N_y \Delta y}. \quad (22)$$

Computing Eq. (20) yields the new wavefront at propagation distance z . For our numerical simulation, the effect of G_2 , with bar width b_2 and pitch g_2 , is simulated in a similar way as was done for G_1 . Moreover, since G_2 is an absorption grating, only one Dirac comb is needed:

$$G_2(x) = \text{comb}\left(\frac{x}{g_2}\right) * \text{rect}\left(\frac{x}{b_2}\right). \quad (23)$$

The effect of this grating on the wavefront is subsequently applied through pointwise multiplication of the propagated wavefront intensity with the 2D extension of $G_2(x)$. In this way, we obtain the final intensity at the detector, required for generating the phase stepping images.

2.4.2. Phase stepping and detection

Finally, for simulating detection of the intensity, a detector pixel size p_d is defined. Since $p_d \geq \Delta x, \Delta y$, the wavefront intensity $|D(x, y)|^2$ is integrated over every detector pixel. Such a detector pixel will overlap with many wavefront pixels, meaning the integration corresponds to a summation over those wavefront pixels that overlap with a certain detector pixel. As a result, phase stepping images are generated by repeatedly shifting the G_2 array (with periodic boundary conditions) over a number of wavefront pixels, corresponding to the desired displacements of the grating. For every shifted position of G_2 , the intensity arriving at the detector is recalculated and a phase stepping image is generated.

2.4.3. Subpixel phase stepping

The discrete nature of the phase stepping procedure in 2.4.2 imposes certain limitations on the accuracy with which the phase stepping can be performed. Indeed, as both the grating and the wavefront are defined on the same discrete grid, the smallest meaningful shift is determined by the pixel size of the grid. The same is true for the definition of the pitch of G_2 .

In some occasions, the desired shift cannot be expressed by an integer number of pixels. Therefore, we propose to use a subpixel phase stepping approach to omit these restrictions. In order to do this in practice, a fractional transmission between 0 and 1 is assigned to every wavefront pixel, rather than exactly 0 or 1 as was done in the pixel based procedure described above.

To determine the correct transmission factor F_{trans} in a certain pixel (x, y) of the wavefront, we propose to calculate the difference $F_{\text{trans}} = P_{G_2}(x_1) - P_{G_2}(x_0)$, where $P_{G_2}(x)$ is given by

$$P_{G_2}(x) = \frac{1}{2\Delta x} \left[\frac{g_2}{4} f_{\text{TW}} \left(\frac{2\pi}{g_2} x \right) + x \right]. \quad (24)$$

Here, it is assumed that x_0 and x_1 are the real world coordinates of the wavefront pixel boundaries along the stepping direction. For convenience, assume $x_0 = 0$ for pixels $(x, y) = (1, y)$. The rationale for this procedure is understood by considering $G_2(x)$ as a modified square wave.

First, assume $f_{\text{SW}}(x)$ denotes a regular square wave as shown in Fig. 4 and given by

$$f_{\text{SW}}(x) = \text{sgn}(\sin x). \quad (25)$$

The primitive function of $f_{\text{SW}}(x)$ is, up to a constant term, given by $(\pi/2)f_{\text{TW}}(x)$ and is also shown in Fig. 4.

Subsequently, we transform $f_{\text{SW}}(x)$ to $G_2(x)$ by adding an offset of 1 and dividing the result by 2. In this way, the square wave has a minimum value of 0 and a maximum value of 1, expressing the

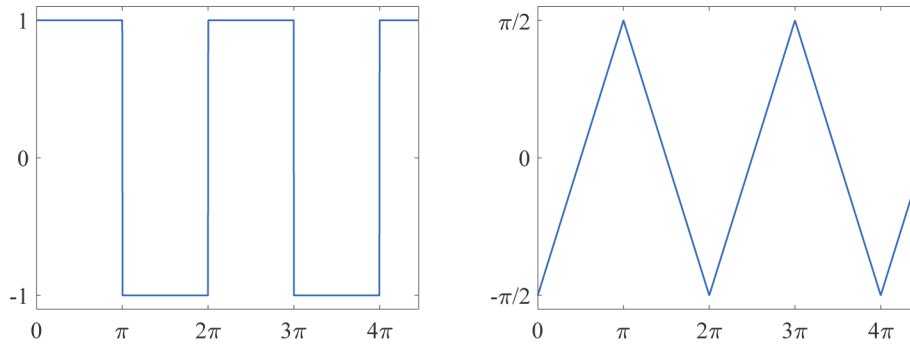


Fig. 4. (left): Square wave with period 2π , mean 0 and amplitude 1. (right): The primitive function of the square wave, up to a constant.

transmission of the grating. The desired periodicity is attained by the transformation $x \rightarrow 2\pi x/g_2$. Therefore, we write

$$G_2(x) = \frac{1}{2} \left[1 + f_{\text{SW}} \left(\frac{2\pi}{g_2} x \right) \right]. \quad (26)$$

In addition, the area under the $G_2(x)$ curve within a pixel must express the transmitted fraction in that pixel. Assume for example that $\Delta x = g_2/2$ and that a certain pixel is perfectly aligned with a transmitting grating line. The surface under the curve in the pixel is then simply the width Δx times 1, yielding a value of Δx . However, as $G_2(x)$ in this pixel is fully transmitting, $G_2(x)$ must be scaled such that this calculation yields 1. In order to achieve this, we scale $G_2(x)$ with a factor $1/\Delta x$:

$$G_2(x) = \frac{1}{2\Delta x} \left[1 + f_{\text{SW}} \left(\frac{2\pi}{g_2} x \right) \right]. \quad (27)$$

Integration yields:

$$\int G_2(x) dx = \frac{1}{2\Delta x} \int dx + \frac{1}{2\Delta x} \int f_{\text{SW}} \left(\frac{2\pi}{g_2} x \right) dx. \quad (28)$$

Since the last term corresponds to the primitive of the square wave, we get

$$\int G_2(x) dx = \frac{1}{2\Delta x} \left[\frac{g_2}{4} f_{\text{TW}} \left(\frac{2\pi}{g_2} x \right) + x \right] + \text{const.} \quad (29)$$

This result equals, up to a constant, $P_{G_2}(x)$ as defined in Eq. (24). The transmitted fraction in a pixel is thus determined by calculating the area under $G_2(x)$ over the range of the pixel, or in other words, by computing the definite integral of $G_2(x)$. By definition, we have:

$$F_{\text{trans}} = \int_{x_0}^{x_1} G_2(x) dx \quad (30)$$

$$= \frac{1}{2\Delta x} \left[\frac{g_2}{4} f_{\text{TW}} \left(\frac{2\pi}{g_2} x_1 \right) + x_1 \right] - \frac{1}{2\Delta x} \left[\frac{g_2}{4} f_{\text{TW}} \left(\frac{2\pi}{g_2} x_0 \right) + x_0 \right] \quad (31)$$

$$= P_{G_2}(x_1) - P_{G_2}(x_0). \quad (32)$$

The integration constants cancel out in the definite integral, and we obtain a straightforward way to precalculate the transmitted fraction in every pixel. Indeed, given that the pixel size Δx is fixed, $F_{\text{trans}}(m, n)$ is simply computed as $F_{\text{trans}}(m, n) = P_{G_2}(m\Delta x) - P_{G_2}([m-1]\Delta x)$. This is evaluated directly for every pixel in the wavefront. The effect of phase stepping is incorporated by shifting $P_{G_2}(x)$ accordingly.

2.5. Alternative wavefront generation using ROOT

When building the wavefront in GATE, the wavefront resolution and number of contributing photons are fixed as soon as the MC simulation is initialised. Changing these parameters thus requires a new simulation. Alternatively, all photon-tracking data generated with GATE, including position, energy, and phase of each photon, can be saved as a tree-structure in ROOT-format [28]. To combine the data holding information about those three parameter, the ROOT environment is used. A ROOT-program written in C++ was applied to the tree-structure in order to coherently add the photon contributions.

An advantage of separating the MC simulation and the wavefront construction, is that the sampling parameters of the wavefront are, in that case, independent of the MC simulation. Changing the wavefront grid size therefore does not require a new MC experiment. Following this approach, however, the output size of the GATE simulations depends on the number of photons, increasing rapidly as more photons are generated. Thus, the gained flexibility comes at the cost of large amounts of intermediate ROOT-data and the inclusion of an additional step in the procedure (three instead of two), where a loop over all photons saved in the ROOT-file is required to build the wavefront. Which of the two aforementioned approaches is the most suitable one therefore highly depends on whether the user requires flexibility or computational efficiency.

3. Experiments

3.1. Validation tests

To validate the performance of our proposed x-ray phase contrast simulator, three distinct tests were run. First, the simulated intensity profile resulting from refracting a parallel 20 keV beam at a spherical phantom in GATE was compared to the theoretically expected profile (as in [10]). The simulated sphere with radius 100 μm was homogeneous, made of water and was assigned $\delta = 2.0 \cdot 10^{-6}$ to ensure a visible refraction effect. In total, $20 \cdot 10^6$ photons were considered in GATE for the generation of the profile.

Subsequently, the phase gained by the photons was compared with the expected result from the theoretical model. For this, a GATE simulation was performed with 10^5 parallel beam photons at 25 keV. Between source and detector, a homogeneous 4 mm \times 4 mm epoxy layer was placed, with a thickness of $d_{\text{epoxy}} = 1$ mm. The detector size was 5 mm \times 5 mm and the expected number of photons travelling through the epoxy layer was therefore approximately $62 \cdot 10^3$.

Finally, the propagation method was tested by propagating a plane wave, starting from the phase grating, assuming 25 keV x-rays and an induced phase-shift of π . The n -th fractional Talbot distance d_n is then given by [17]:

$$d_n = n \frac{g_1^2}{8\lambda}, \quad (33)$$

where g_1 is the grating pitch, which was assumed to be 4 μm . The pattern was simulated up until the 7th fractional Talbot distance.

3.2. Radiography

In this section, the simulation of a 2D radiograph is demonstrated, using the described workflow. Prior to discussing the simulation, the GATE phantom used in this simulation is briefly described.

3.2.1. Phantom

The phantom was a simplified model for a carbon fiber reinforced polymer (CFRP), which is an advanced composite material used in many industrial applications. A CFRP consists out of a number of bundles of carbon fibers, embedded in a resin, often epoxy. The combination of low density materials and strongly ordered microstructures makes CFRPs interesting objects for

XPC (including DFC) imaging. For our experiments, a phantom was constructed containing 12 fiber bundles, arranged in layers with pairs of two. Bundles in the same layer were parallel and the orientation in each layer alternates between horizontal and vertical. The cross section of the bundles was elliptical in shape with short and long axes lengths of $112.5 \mu\text{m}$ and $675 \mu\text{m}$, respectively, and the resin material was epoxy. The phantom as represented in GATE is shown in Fig. 5.

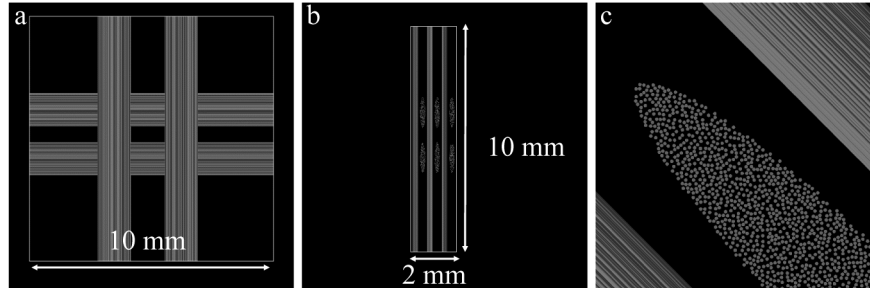


Fig. 5. CFRP phantom as seen in GATE, showing a front view (a), side view (b) and a zoomed in image (c). A central FOV of $5 \text{ mm} \times 5 \text{ mm}$ of the front view is used for the simulation.

For practical reasons, the size was limited in terms of thickness (2 mm) and field of view ($5 \text{ mm} \times 5 \text{ mm}$). In order to take the small angle scatter into account, the microstructure was modelled down to the scale of individual carbon fibers [29]. The number of fibers in a bundle was determined through the number density ρ_N :

$$\rho_N = \left(\frac{1}{\pi r_f^2} \right) \left(1 + \frac{\rho_f}{\rho_r} \left(\frac{1}{c_f} - 1 \right) \right)^{-1}. \quad (34)$$

Here, r_f is the radius of a single fiber, ρ_f the mass density of the fiber material, ρ_r the resin mass density, and c_f the carbon fiber weight fraction. The positioning of the fibers in the bundle was done in a randomized way, allowing the generation of 12 unique bundles for the phantom. Assuming a weight fraction of 0.60 and a fiber radius of $3.5 \mu\text{m}$, this resulted in approximately 2570 fibers per bundle, of which the positions were determined by Poisson disc sampling [29]. The phantom as a whole contained over 30,000 individual fibers. Given that the dark field signal is orientation dependent [2], we expect to observe differences between horizontal and vertical fiber bundles in the simulation result.

If the fibers are modeled as perfectly smooth cylinders in GATE, the refraction at each individual fiber will generate an intensity profile similar to the one shown in Fig. 7. The superposition of many of these perfect refraction events can, due to the low overall absorption of the phantom materials, result in artefacts as the positive peaks at the edges will dominate the contrast. This can be resolved by introducing surface roughness of the fibers as discussed in 2.3.2. Surface roughness is a contributing factor in the CFRP manufacturing process, making it a relevant feature for our simulation model [30,31]. Despite the fact that this model is strictly speaking not completely accurate with respect to individual fibers, we argue that it suffices for our goals, as the most important effect of the surface roughness is taken into account. The scale at which we expect the local surface normal variations to occur is submicrometer [32], and the potential differences between using the stochastic model and using a well defined map of local variations is therefore unlikely to have any effect on the global result. Furthermore, it should be noted that the error propagation in this case does not differ from that of conventional Geant4. The surface roughness model essentially just adds a randomisation to a computational step that would occur anyway, namely the calculation of the surface normal vectors at the intersection points.

3.2.2. Simulation

The simulation was performed in GATE with $250 \cdot 10^9$ parallel beam photons at an energy of 25 keV. For the wave propagation, a π -shifting phase grating with a pitch of $4 \mu\text{m}$ was chosen. The matching absorption grating at the first fractional Talbot distance therefore had a pitch of $2 \mu\text{m}$ [17]. The wavefront pixel size was set to $0.1 \mu\text{m} \times 0.1 \mu\text{m}$ to keep the sampling well below the fiber size, resulting in a $50,000 \times 50,000$ grid. For the GATE simulation, we used the Hopper HPC cluster installed at the University of Antwerp (<https://www.uantwerpen.be/en/core-facilities/calcula/infrastructure/>). The wave propagation part was performed on a local server with 16 (dual) cores. While performing the phase stepping, images were collected from the $50,000 \times 50,000$ grid on a 250×250 detector. These phase stepping images were subsequently inserted in the phase retrieval algorithm (see Section 2.1) to finally yield the transmission image, visibility map (DFC) and DPC image.

In addition, a second radiography simulation was performed. The experimental conditions were identical to those in the simulation described above, but with a slightly tilted phantom (rotation around the optical axis). As was already mentioned, the dark field contrast is orientation dependent, meaning the simulation results with a rotated phantom are expected to differ from those of the previously described experiment, despite the fact that experimental conditions and phantom were identical.

3.3. Computed tomography

In the following, the simulation of sinograms for CT is demonstrated, using the described workflow. We limited the study to 2D sinograms to keep the computation times reasonable. As was done in Section 3.2, a brief description of the phantom used in the simulation is given prior to demonstrating our results. For the tomographic reconstruction of the simulated sinograms, the open source ASTRA-toolbox was used [33–35].

3.3.1. Phantom

The phantom used for the CT simulation, which is also based on CFRP properties, is shown in Fig. 6. This phantom contained three cylinders consisting of carbon. Two cylinders, one with a radius of 1 mm and one with a radius of $150 \mu\text{m}$, were solid, whereas the third cylinder, also having a $150 \mu\text{m}$ radius, was filled with 700 fibers with radius $3.5 \mu\text{m}$ to simulate microstructure. These fibers were identical to those in Section 3.2.1 and were positioned following the same position sampling procedure. The three cylinders were embedded in an epoxy cylinder (radius 5 mm). Since the solid cylinders were homogeneous, the DFC signal is expected to be small. The fiber bundle, on the contrary, is expected to induce a strong DFC signal. In real XPC experiments, DFC reconstructions are a valuable tool, for example to determine fiber orientations inside a sample.

3.3.2. Simulation

In the simulation experiments, $30 \cdot 10^9$ photons were simulated in a parallel beam in GATE at an energy of 25 keV. For the wave propagation, we assumed a π -shifting phase grating (G_1) with a pitch of $4 \mu\text{m}$. The matching absorption grating (G_2) at the first fractional Talbot distance therefore had a pitch of $2 \mu\text{m}$. To investigate the effect of surface roughness on the AC image, sinograms were simulated both with and without surface roughness. For each of the two simulations, 200 equiangular projections were simulated over an angular range of 180° . Five phase steps were simulated for every orientation.

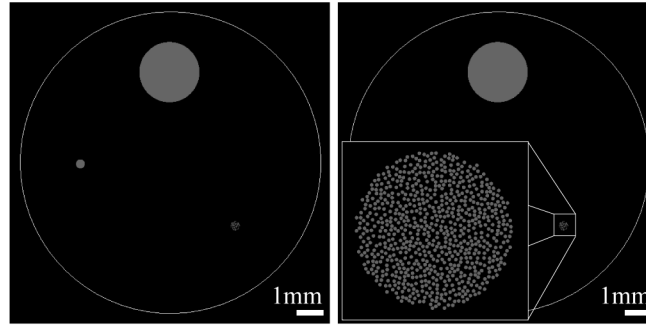


Fig. 6. GATE phantom used for the CT simulation.

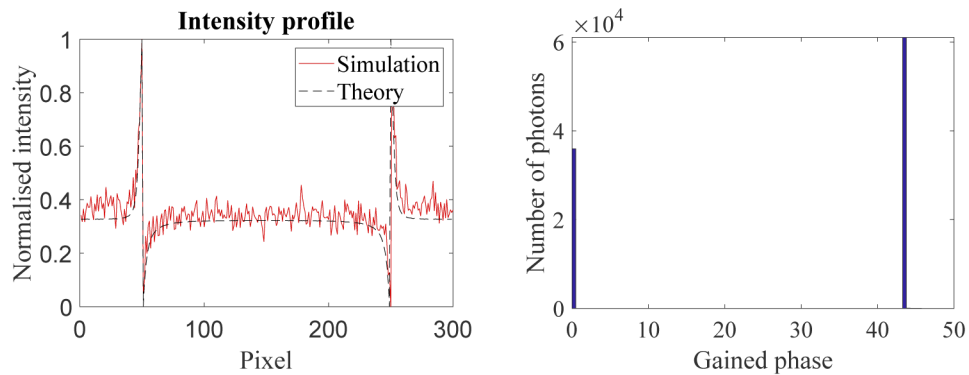


Fig. 7. (left): Simulated and theoretical normalised intensity profiles resulting from refraction at a spherical phantom with $\delta = 2.0 \cdot 10^{-6}$. (right): Phase gained by 10^5 parallel beam photons at 25 keV, of which a subset of 62% crossed a 1 mm thick epoxy layer with $\delta_{\text{epoxy}} = 3.43593 \cdot 10^{-7}$.

4. Results

4.1. Validation tests

The theoretical [10] as well as the simulated intensity profile are shown in Fig. 7, where the 300 pixels are each $1 \mu\text{m}$ wide. As can be observed from that figure, the simulated results match the theoretical expectations. The fluctuations in the simulated profile are due to the photon statistics resulting from the MC simulation. The simulation was performed with a 300×300 pixels detector. This means that, on average, we would expect each background pixel to collect about 200 photons. Increasing this number by simulating more photons at the source would lower the noise in the intensity profile, at the cost of a longer simulation time. The results of the simulation with the epoxy layer are shown in Fig. 7. From the model and the fact that $\delta_{\text{epoxy}} = 3.43593 \cdot 10^{-7}$ at 25 keV, the gained phase was expected to be $\Delta\phi = k_p \delta_{\text{epoxy}} d_{\text{epoxy}} = 43.5$. It can be seen that the simulation results in a correct fraction of photons with the expected phase gain, being 43.5. The other photons have not crossed the phantom and thus did not gain any phase, expressed by the peak at a phase gain of zero. This demonstrates that the phase gained during the simulation corresponds to the theoretically predicted phase.

Finally, the wave propagation was evaluated. As expected, a Talbot carpet is observed when visualising the wavefront intensity as a function of the distance from the grating. The resulting pattern is shown up to the 7th fractional Talbot distance in Fig. 8, covering a field of view of

approximately $20 \mu\text{m} \times 200 \text{mm}$. The pattern matches the Talbot distances calculated from Eq. (1), indicated on the horizontal axis.

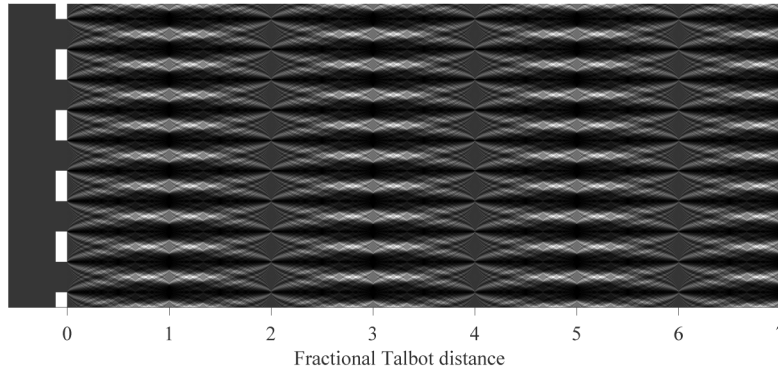


Fig. 8. Simulated wavefront intensity up to the 7th fractional Talbot distance for a 25 keV plane wave after interaction with a $4 \mu\text{m}$ pitch π -shifting grating.

4.2. Radiography

The final images of the CFRP phantom with horizontal and vertical bundles (after phase retrieval) are shown in Fig. 9. Note that the horizontal fiber bundles are not visible in the DFC and DPC images. This is because the fiber bundles are oriented perpendicular to the grating bars, and the interferometer is only sensitive to phase variations perpendicular to the bar orientation. In contrast to the horizontal bundles, the vertical fiber bundles are clearly visible in both DPC and DFC. The internal structure of the fiber bundles shows in all contrasts. Note that the DPC image suffers from phase retrieval artefacts caused by the scattering at the fibers [3,29]. The DFC signal is clearly lowered because of scattering in the vertical bundle.

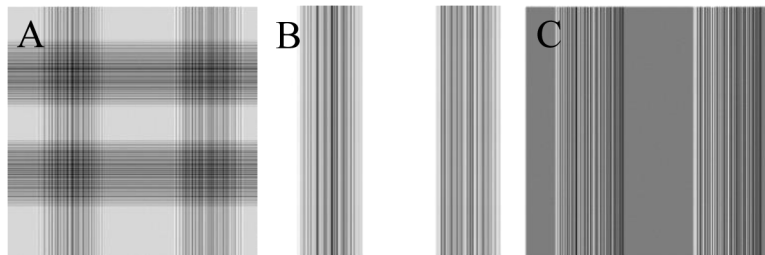


Fig. 9. Simulated images for the CFRP phantom shown in Fig. 5. A) transmission image, B) DFC image, and C) DPC image. The horizontally oriented fiber bundle is not visible in the DFC and DPC images.

Furthermore, the dark field signal or visibility is known to be dependent on the so-called autocorrelation length of the grating-interferometer setup [36–38]. The dependency is related to the size and shape of the scattering structures in the object. Microspheres are a well studied case [38]. To demonstrate this effect, the simulated radiograph from the phantom shown in Fig. 5 was obtained for three different propagation distances: the first, third and fifth fractional Talbot distance. In Fig. 10, we demonstrate the evolution of the visibility while increasing the propagation distance, hereby effectively changing the autocorrelation length of the simulated setup [38]. The notable decrease in visibility with increasing propagation distance clearly

indicates that the dark field signal indeed shows a strong dependency on the autocorrelation length.

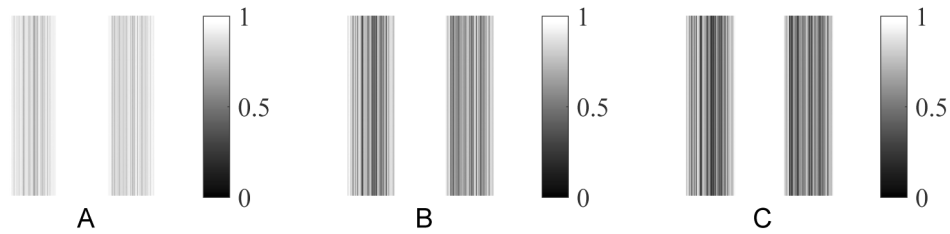


Fig. 10. Simulated visibility for the phantom shown in Fig. 5, acquired at A) the first fractional Talbot distance, B) the third fractional Talbot distance, and C) the fifth fractional Talbot distance. Note that the scaling of the grey values in these images differs from the scaling in Fig. 9.

In the second simulation, the fiber bundles were slightly rotated, tilting them away from their perfectly horizontal and vertical orientations. The corresponding images are shown in Fig. 11. As can be observed, the horizontal bundles now show up in both the DPC and the DFC image. A more faint appearance is observed however, in comparison to the vertical bundles, as the latter still resulted in a stronger phase variation and scatter component along the sensitivity direction of the simulated interferometer. As can be seen in the images, the discretization of the tilted bundles on the 250×250 grid has caused visual degradation in the images.

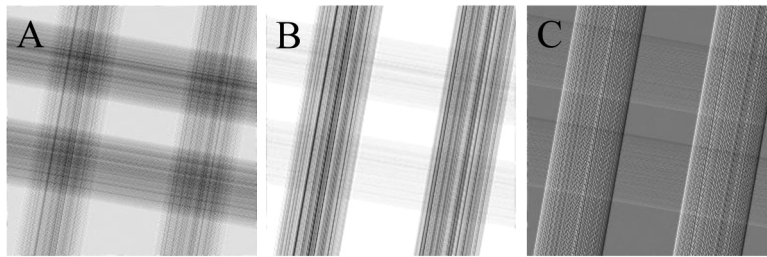


Fig. 11. Simulated images for the CFRP phantom shown in Fig. 5, but with a slightly tilted phantom. A) transmission image, B) DFC image, and C) DPC image. The horizontally oriented fiber bundle is now visible in the DFC and DPC images.

4.3. Computed tomography

The simulated projection data (sinograms) with surface roughness, resulting from the phase retrieval, are shown in Fig. 12.



Fig. 12. Simulated sinograms for A) absorption contrast; B) differential phase contrast; and C) dark field contrast.

From the DFC sinogram, it is immediately clear that the cylinder with microstructure yields a strong dark field signal due to the small angle scatter of the X-rays. As the cylinder edges reflect X-rays, the coherence is also locally disturbed and they show up in the dark field sinogram for the larger cylinders. In the DPC sinogram, the edge enhancement effect is also visible. From the sinogram, tomographic images, shown in Fig. 13, were reconstructed with the ASTRA toolbox.

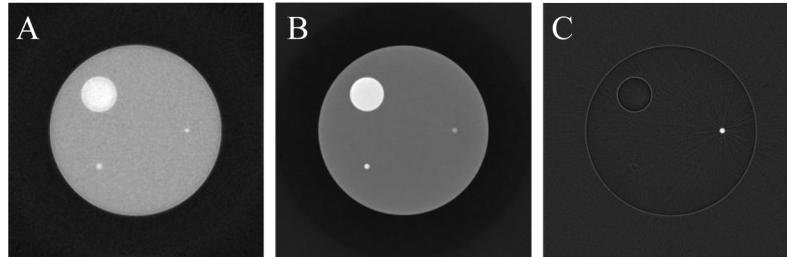


Fig. 13. CT reconstructions of the sinograms shown in Fig. 12.

As expected from the sinogram, the fiber bundle gives a strong dark field signal in the CT reconstruction. In addition, the edges of the cylinders are enhanced in the DFC image. Slight differences are visible between the smaller solid cylinder and the fiber bundle in both the absorption and the phase contrast reconstruction. As the reconstructed phase contrast image is no longer proportional to the derivative of the phase shift, the edge enhancement disappears after reconstruction. The AC sinogram and reconstruction from the simulation without surface roughness are shown in Fig. 14.

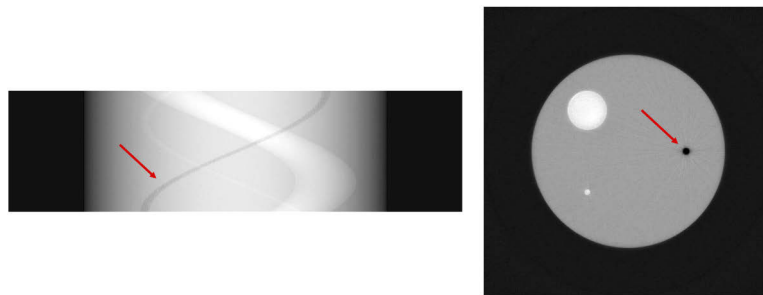


Fig. 14. Simulated AC sinogram and corresponding tomographic reconstruction for the phantom described in Section 3.3.1, without surface roughness of the fibers. The red arrow indicates the affected fiber bundle in both the sinogram and the reconstruction.

To illustrate how the computation time scales with the complexity of the phantom, the plot in Fig. 15 shows the computation time for a simulation with 10^6 photons for a total amount of fibers ranging from 100 to 30 000. The latter being the approximate number of fibers in the phantom used for the radiographs. The following data points were collected: 100, 500, 1000, 2000, 5000, 10 000, 15 000, 20 000, 25 000, and 30 000 fibers. From the plot, a linear increase in computation time can be observed. For clarity, only the MC computation time was considered, as the time required for the wavefront propagation is independent of the number of fibers in the phantom.

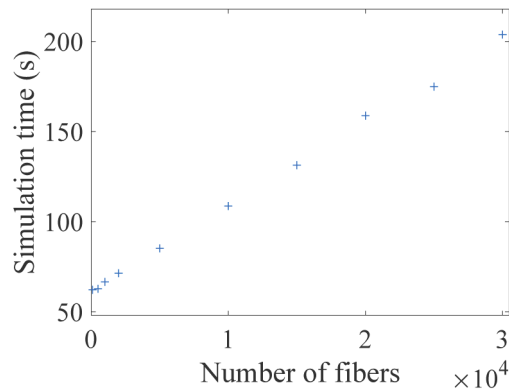


Fig. 15. Computation time for the MC simulation for a constant number of 10^6 photons, but a varying amount of fibers in the phantom.

5. Discussion

The validation tests demonstrate the correctness of the key simulation elements: photon refraction (Fig. 7), phase shifting (Fig. 7), and wavefront propagation (Fig. 8). In Fig. 7, the refraction introduces a positive and a negative peak at the phantom edge, since photons are deflected outwards. As the intensity scales with the square of the number of photons, the contrast between the increased number of photons outside and the decreased number of photons inside the sphere becomes amplified when plotting the intensity rather than the counts. Indeed, the positive peak in Fig. 7 is significantly larger than its negative counterpart. Two properties contribute to the magnitude of the observed peaks in the intensity profile: monochromaticity and surface smoothness. A reduction in either of those is expected to potentially smear out the peaks, as in both cases the spread in photon propagation directions increases. Simulation experiments (not shown here) revealed that the effect of polychromaticity is negligible, based on which we decided to focus on introducing surface roughness in the simulations. The simulated radiographs in Fig. 9 and Fig. 11, show that our GATE-based XPC simulation framework is indeed able to generate the different types of contrast: the transmission image shows the higher absorption in the fiber bundles, whereas the invisible horizontal bundles in the DPC and DFC images reflect the absence of scatter and phase gradient along the x -direction in those bundles, respectively. The fiber bundles in the phantom do appear non-smooth in the images. This is explained by the fact that, for our parallel beam geometry, projecting the $5 \text{ mm} \times 5 \text{ mm}$ FOV on a 250×250 detector results in each pixel representing $20 \mu\text{m} \times 20 \mu\text{m}$ of the FOV. As the fibers are $7 \mu\text{m}$ in diameter, this caused the structure of the superposed fiber bundles to show through in the images. In addition, as the fibers are perfectly straight in this simulation, the discretization on the detector pixel grid is expected to introduce partial volume or aliasing effects. These effects are apparent in Fig. 11.

The sinogram data in Fig. 12 show the expected absorption effects. In the DPC and DFC images, the expected edge enhancement is present. Furthermore, the DFC signal of the fiber bundle is very strong. The CT reconstructions in Fig. 13 show similar streaking and edge effects in the DFC image, as reported by Peter et al. [13], although the phantom used in that study was not specifically focussed on CFRP properties. The difference between epoxy (matrix) and carbon (cylinders and fibers) is visible in both the AC and DPC images. For the CT simulation, the detector pixel size was $50 \mu\text{m}$, which is significantly larger than the fiber diameter, resulting in less aliasing effects in comparison to the radiographs of Section 4.2.

Surface roughness was taken into account through a stochastic model, which ignores the specific surface of individual fibers but allows to simulate the general effect the roughness has on the projection data in a computationally efficient way. In Fig. 14, the AC sinogram and its tomographic reconstruction are shown for a simulation with the phantom from Section 3.3.1, but without introducing surface roughness. In other words, the individual fibers are all perfectly smooth. As can be seen from the figure, the absorption contrast in the fiber bundle is severely impacted. This effect can be understood from the intensity profile shown in Fig. 7. Towards the edges of the sphere, the intensity drops at the inner side of the edge, while a positive peak appears just outside of the sphere. These peaks are present because photons are refracted away from the sphere [10].

The same effect occurs in the individual fibers in the fiber bundle, and this is the origin of the unwanted effect shown in Fig. 14. Indeed, since the phantom contains over 700 fibers, a superposition of many of these amplified intensity peaks is created. Due to this effect, the average intensity originating from the fiber bundle is expected to be higher compared to the same amount of material but concentrated in a single cylinder. For strongly absorbing phantoms, this effect might go unnoticed. The phantom used in this study for the CT simulation however, consists of only low absorbing materials. This allows the effect to dominate the contrast, hereby severely underestimating the absorption. In this case, the underestimation leads to an apparent drop in attenuation at the fiber bundle in the tomographic reconstruction, as seen in Fig. 14.

Recently, an advanced digital phantom was presented by Sung et al. to demonstrate the phase contrast simulation of a human thorax based on a full wave simulation approach [39]. To this end, the authors assumed the refractive index of the phantom to change gradually within the imaged object and at the boundaries, allowing the use of an approximated solution to the wave equation known as the first Rytov approximation [40,41]. Their work is primarily oriented towards free-space propagation phase contrast imaging, however a procedure for combining the calculated attenuation and phase maps to generate a differential phase contrast image was also demonstrated. As opposed to the method presented in our work, this did not include modelling of the interferometer. An advantage of incorporating the interferometer explicitly in the simulation, is that this allows analysis of the phase stepping images, which are of interest when exploring phase retrieval methods. In [40], the possibility of using the full wave approach as a forward model for tomography is briefly discussed. Given the computational requirements inherent to the MC part of our work, it is practically unfeasible to use our presented tool for this same purpose. On the other hand, the MC part allows for detailed modelling of photon-matter interactions such as Compton scatter and photoelectric absorption, relying on their respective physical cross sections. Furthermore, tracking the individual refraction events of photons at microstructures is an important feature of the MC part for accurate modelling of the small angle scatter underlying the dark field image formation process. By passing the output of the MC part to the wave optics part, both particle and wave properties are present in the simulations. Dark field contrast images were not simulated in [39] and details smaller than approximately $125\ \mu\text{m}$ were not (yet) included in their phantom, whereas microstructures well below $10\ \mu\text{m}$ were taken into account in our work to simulate small angle scattering. It should, however, be noted that, while the work presented in [39] focuses on the phase contrast modality, our work intends to explore the dark field contrast modality as well, which could explain the difference in presented methodology. Indeed, an as accurate as possible phase contrast image at a human scale clearly benefits from exploiting the wave properties to a maximum, whereas a Monte Carlo approach is more suited for the detailed modelling of the small angle scatter underlying the dark field contrast. The latter is also gaining increasing interest with respect to medical applications such as lung imaging [42].

Several improvements to our simulation framework can be considered. Firstly, we did not focus on incoherent radiation and the need of grating G_0 for lab-based cone beam sources. Adequate modelling of G_0 as part of the MC simulation requires interference effects to be considered

explicitly in the MC part [11] and was out of scope of this study. Secondly, polychromaticity was not included in the simulation experiments. Although not shown, it can easily be taken into account in the propagation part of the framework by integrating over the energy spectrum [8]. Lastly, MC simulations are notoriously known to be computationally expensive and our simulation framework is no exception. Adding additional refraction interactions to every photon trajectory certainly prolongs the simulation time. Despite our efforts to at least reduce the data output storage requirements (Section 2.4) and the use of a computer cluster, this is still a major limitation. Improving the computational efficiency is, therefore, important future work. An efficient GPU implementation of the simulation code could therefore substantially decrease the computation time. Despite the abovementioned shortcomings, the results shown in this study demonstrate the ability of our simulation framework to generate phase contrast CT projection data of realistic phantoms, paving the way for simulation studies on phase contrast system design, acquisition strategies, phase retrieval and reconstruction.

6. Conclusion

In this work, we extended GATE, a framework for Monte Carlo based medical imaging simulations, with novel tools to simulate X-ray phase contrast imaging. The GATE output was post-processed for wave front propagation to allow grating-based imaging. The implementation was validated by comparing the simulation results to the expected theoretical results and we found these to be matching. Furthermore, 2D radiography simulations were presented as well as sinogram simulations for CT reconstruction. Realistic CFRP phantoms were designed and it was shown that the resulting simulations exhibit the relevant properties of an actual CFRP sample, demonstrating that the framework can generate the most important effects in phase and dark field imaging. To our best knowledge, this is the first time a 2D dark field image for a CFRP-like phantom was simulated with such detailed fiber modelling at this scale (5 mm \times 5 mm FOV).

A. Triangle wave phase retrieval

In the absence of grating and detector imperfections, polychromaticity, and incoherence, the phase stepping curve is described by a triangular model. Hence, a triangular wave form (cfr Eq. (3)) was fitted to the measured phase stepping points following a least squares optimization procedure. For simplicity, we consider only a single pixel and therefore omit the explicit notation of pixel indices (i, j) . Since proper initialization of the parameters a_0 , a_1 and ϕ_1 generally improves the optimization performance, we will first describe an automated procedure for finding such starting values.

Suppose that only four measurements (four steps) are available, sampled over a single period of the phase stepping curve, for initial estimation of the three parameters of a triangle wave. First, as a single period of a triangle wave shows either two or three consecutive slopes, at least two of these four measurements are situated on the same slope. This means that one of the slopes can be easily estimated and, as a result, all other slopes are also known. It is not immediately known which points lie on the same slope, but this is deduced by calculating the slopes between adjacent measurements. Indeed, the points lying on the same slope are found by extracting the steepest slope from the set of calculated slopes, as the slope connecting points lying on a different side of the triangle will always be less steep.

Having assigned the same slope to these two points residing on the same side of the triangle, the slope for the neighbouring points can be computed. If we connect a neighbouring point to the last known point, and the slope corresponds to the one found for the known point, the neighbouring point is assumed to lie on the same side and is assigned the same slope. If no correspondence can be found, the neighbouring point must lie on the other side of the triangle and therefore is assigned the opposite slope. Using periodic boundary conditions, the first and last point in the series can also be considered to be neighbours. Generally speaking, due to the periodicity, every

point can be shifted by $\pm 2\pi$, allowing to move it to an equivalent position that is closer to its neighbour than π . This means that, in case the adjacent measurements are more than π apart, we find the equivalent position at the same side of the triangle as the neighbouring point. In this way, we are able to assign a slope to every point.

Subsequently, the points and slopes are used to find an estimate of the height and position of the extrema of the phase stepping curve. These estimates are the crucial element for finding the starting values, as the position of the peak leads to an estimate of the phase shift ϕ_1 , whereas the mean of the extrema yields an estimate of a_0 , which in turn leads to an estimate of the amplitude a_1 . This searching procedure is fully automated, and leads to appropriate starting values for the fitting procedure.

Funding

Fonds Wetenschappelijk Onderzoek (G090020N, G094320N, S003421N); Interreg (0386).

Acknowledgments

The computational resources and services used in this work were provided by the HPC core facility CalcUA of the Universiteit Antwerpen, and VSC (Flemish Supercomputer Center), funded by the Research Foundation - Flanders (FWO) and the Flemish Government.

Disclosures

The authors declare that there are no conflicts of interest related to this article

References

1. M. Endrizzi, "X-ray phase-contrast imaging," *Nucl. Instrum. Methods Phys. Res., Sect. A* **878**, 88–98 (2018).
2. T. Jensen, M. Bech, O. Bunk, T. Donath, C. David, R. Feidenhans'l, and F. Pfeiffer, "Directional x-ray dark-field imaging," *Phys. Med. Biol.* **55**(12), 3317–3323 (2010).
3. M. Bech, T. Jensen, O. Bunk, T. Donath, C. David, T. Weitkamp, G. Le Duc, A. Bravin, P. Cloetens, and F. Pfeiffer, "Advanced contrast modalities for x-ray radiology: Phase-contrast and dark-field imaging using a grating interferometer," *Z. Med. Phys.* **20**(1), 7–16 (2010).
4. F. Pfeiffer, T. Weitkamp, O. Bunk, and C. David, "Phase retrieval and differential phase-contrast imaging with low-brilliance x-ray sources," *Nat. Phys.* **2**(4), 258–261 (2006).
5. G. Santin, D. Strul, D. Lazaro, L. Simon, M. Krieguer, M. Martins, V. Breton, and C. Morel, "GATE: A Geant4-based simulation platform for PET and SPECT integrating movement and time management," *IEEE Trans. Nucl. Sci.* **50**(5), 1516–1521 (2003).
6. S. Agostinelli, J. Allison, K. Amako, J. Apostolakis, H. Araujo, P. Arce, M. Asai, D. Axen, S. Banerjee, G. Barrand, F. Behner, L. Bellagamba, J. Boudreau, L. Broglia, A. Brunengo, H. Burkhardt, S. Chauvie, J. Chuma, R. Chytrcek, G. Cooperman, G. Cosmo, P. Degtyarenko, A. Dell'Acqua, G. Depaola, D. Dietrich, R. Enami, A. Feliciello, C. Ferguson, H. Fesefeldt, G. Folger, F. Foppiano, A. Forti, S. Garelli, S. Giani, R. Giannitrapani, D. Gibin, J. Gomez Cadenas, I. Gonzalez, G. Gracia Abril, G. Greeniaus, W. Greiner, V. Grichine, A. Grossheim, S. Guatelli, P. Gumplinger, R. Hamatsu, K. Hashimoto, H. Hasui, A. Heikkinen, A. Howard, V. Ivanchenko, A. Johnson, F. Jones, J. Kallenbach, N. Kanaya, M. Kawabata, Y. Kawabata, M. Kawaguti, S. Kelner, P. Kent, A. Kimura, T. Kodama, R. Kokoulin, M. Kossov, H. Kurashige, E. Lamanna, T. Lampen, V. Lara, V. Lefebvre, F. Lei, M. Liendl, W. Lockman, F. Longo, S. Magni, M. Maire, E. Medernach, K. Minamimoto, P. Mora de Freitas, Y. Morita, K. Murakami, M. Nagamatu, R. Nartallo, P. Nieminen, T. Nishimura, K. Ohtsubo, M. Okamura, S. O'Neale, Y. Oohata, K. Paech, J. Perl, A. Pfeiffer, M. Pia, F. Ranjard, A. Rybin, S. Sadilov, E. di Salvo, G. Santin, T. Sasaki, N. Savvas, Y. Sawada, S. Scherer, S. Sei, V. Sirotenko, D. Smith, N. Starkov, H. Stoecker, J. Sulkimo, M. Takahata, S. Tanaka, E. Tcherniaev, E. Safai Tehrani, M. Tropeano, P. Truscott, H. Uno, L. Urban, P. Urban, M. Verderi, A. Walkden, W. Wander, H. Weber, J. Wellisch, T. Wenaus, D. Williams, D. Wright, T. Yamada, H. Yoshida, and D. Zschesche, "GEANT4 - a simulation toolkit," *Nucl. Instrum. Methods Phys. Res., Sect. A* **506**(3), 250–303 (2003).
7. S. Jan, D. Benoit, E. Becheva, T. Carlier, F. Cassol, P. Descourt, T. Frisson, L. Grevillot, L. Guigues, L. Maigne, C. Morel, Y. Perrot, N. Rehfeld, D. Sarrut, D. Schaart, S. Stute, U. Pietrzyk, D. Visvikis, N. Zahra, and I. Buvat, "GATE V6: A major enhancement of the GATE simulation platform enabling modelling of CT and radiotherapy," *Phys. Med. Biol.* **56**(4), 881–901 (2011).
8. T. Weitkamp, "XWFP: An x-ray wavefront propagation software package for the IDL computer language," *Proc. SPIE* **5536**, 181–189 (2004).

9. A. Malecki, G. Potdevin, and F. Pfeiffer, "Quantitative wave-optical numerical analysis of the dark-field signal in grating-based x-ray interferometry," *EPL* **99**(4), 48001 (2012).
10. Z. Wang, Z. Huang, L. Zhang, Z. Chen, and K. Kang, "Implement x-ray refraction effect in Geant4 for phase contrast imaging," in *IEEE Nuclear Science Symposium Conference Record*, (IEEE, 2009), pp. 2395–2398.
11. S. Cipiccia, F. Vittoria, M. Weikum, A. Olivo, and D. Jaroszynski, "Inclusion of coherence in Monte Carlo models for simulation of x-ray phase contrast imaging," *Opt. Express* **22**(19), 23480–23488 (2014).
12. P. Bartl, J. Durst, W. Haas, T. Michel, A. Ritter, T. Weber, and G. Anton, "Simulation of x-ray phase-contrast imaging using grating-interferometry," in *IEEE Nuclear Science Symposium Conference Record*, (IEEE, 2009), pp. 3577–3580.
13. S. Peter, P. Modregger, M. Fix, W. Volken, D. Frei, P. Manser, and M. Stampanoni, "Combining Monte Carlo methods with coherent wave optics for the simulation of phase-sensitive x-ray imaging," *J. Synchrotron Radiat.* **21**(3), 613–622 (2014).
14. J. Vignero, N. Marshall, K. Bliznakova, and H. Bosmans, "A hybrid simulation framework for computer simulation and modelling studies of grating-based x-ray phase-contrast images," *Phys. Med. Biol.* **63**(14), 14NT03 (2018).
15. T. Weitkamp, A. Diaz, C. David, F. Pfeiffer, M. Stampanoni, P. Cloetens, and E. Ziegler, "X-ray phase imaging with a grating interferometer," *Opt. Express* **13**(16), 6296–6304 (2005).
16. M. Engelhardt, C. Kottler, O. Bunk, C. David, C. Schroer, J. Baumann, M. Schuster, and F. Pfeiffer, "The fractional Talbot effect in differential x-ray phase-contrast imaging for extended and polychromatic x-ray sources," *J. Microsc.* **232**(1), 145–157 (2008).
17. T. Weitkamp, C. David, C. Kottler, O. Bunk, and F. Pfeiffer, "Tomography with grating interferometers at low-brilliance sources," in *Developments in X-Ray Tomography V*, U. Bonse, ed. (SPIE, 2006), pp. 249–258.
18. J. F. Clauser and M. W. Reinsch, "New theoretical and experimental results in Fresnel optics with applications to matter-wave and X-ray interferometry," *Appl. Phys. B* **54**(5), 380–395 (1992).
19. K. Creath, "Phase-measurement interferometry techniques," in *Progress in Optics*, vol. 26 E. Wolf, ed. (Elsevier, 1988), pp. 349–393.
20. T. Weber, P. Bartl, F. Bayer, J. Durst, W. Haas, T. Michel, A. Ritter, and G. Anton, "Noise in x-ray grating-based phase-contrast imaging," *Med. Phys.* **38**(7), 4133–4140 (2011).
21. A. Momose, W. Yashiro, Y. Takeda, Y. Suzuki, and T. Hattori, "Phase tomography by x-ray Talbot interferometry for biological imaging," *Jpn. J. Appl. Phys.* **45**(6A), 5254–5262 (2006).
22. J. Sanctorem, J. De Beenhouwer, and J. Sijbers, "X-ray phase-contrast simulations of fibrous phantoms using GATE," in *2018 IEEE Nuclear Science Symposium and Medical Imaging Conference (NSS/MIC)*, (IEEE, 2018), pp. 1–5.
23. B. Henke, E. Gullikson, and J. Davis, "X-ray interactions: Photoabsorption, scattering, transmission, and reflection at $E = 50\text{--}30,000$ eV, $Z = 1\text{--}92$," *At. Data Nucl. Data Tables* **54**(2), 181–342 (1993).
24. J. De Beenhouwer, S. Staelens, S. Vandenberghe, J. Verhaeghe, R. Van Holen, E. Rault, and I. Lemahieu, "Physics process level discrimination of detections for GATE: Assessment of contamination in SPECT and spurious activity in PET," *Med. Phys.* **36**(4), 1053–1060 (2009).
25. D. C. O'Shea, *Diffraction Optics - Design, Fabrication, and Test* (SPIE, 2004).
26. J. W. Goodman, *Introduction to Fourier Optics* (McGraw-Hill, 1996).
27. M. Bartels, *Cone-beam x-ray phase contrast tomography of biological samples* (Universität Göttingen, 2013).
28. R. Brun and F. Rademakers, "ROOT - An object oriented data analysis framework," *Nucl. Instrum. Methods Phys. Res., Sect. A* **389**(1-2), 81–86 (1997).
29. J. Sanctorem, J. D. Beenhouwer, J. Weissenböck, C. Heinzl, J. Kastner, and J. Sijbers, "Simulated grating-based x-ray phase contrast images of CFRP-like objects," presented at the *9th Conference on Industrial Computed Tomography (iCT)*, Padova, Italy, 13-15 Feb. 2019.
30. Y. Yao and S. Chen, "The effects of fiber's surface roughness on the mechanical properties of fiber-reinforced polymer composites," *J. Compos. Mater.* **47**(23), 2909–2923 (2013).
31. G. Wu, L. Ma, and H. Jiang, "The roles of surface wettability and roughness of carbon fibers in interfacial enhancement of silicone resin composites," *Polym. Compos.* **40**(S1), E255–E264 (2019).
32. B. N. Zaitsev, N. I. Baklanova, and T. M. Zima, "Atomic force microscopy study of surface-modified carbon fibers," *Inorg. Mater.* **44**(6), 592–597 (2008).
33. W. J. Palenstijn, K. J. Batenburg, and J. Sijbers, "Performance improvements for iterative electron tomography reconstruction using graphics processing units (GPUs)," *J. Struct. Biol.* **176**(2), 250–253 (2011).
34. W. van Aarle, W. J. Palenstijn, J. De Beenhouwer, T. Altantzis, S. Bals, K. J. Batenburg, and J. Sijbers, "The ASTRA Toolbox: A platform for advanced algorithm development in electron tomography," *Ultramicroscopy* **157**, 35–47 (2015).
35. W. van Aarle, W. J. Palenstijn, J. Cant, E. Janssens, F. Bleichrodt, A. Dabrovolski, J. De Beenhouwer, K. J. Batenburg, and J. Sijbers, "Fast and flexible X-ray tomography using the ASTRA toolbox," *Opt. Express* **24**(22), 25129–25147 (2016).
36. W. Yashiro, Y. Terui, K. Kawabata, and A. Momose, "On the origin of visibility contrast in x-ray Talbot interferometry," *Opt. Express* **18**(16), 16890 (2010).
37. S. K. Lynch, V. Pai, J. Auxier, A. F. Stein, E. E. Bennett, C. K. Kemble, X. Xiao, W.-K. Lee, N. Y. Morgan, and H. Harold Wen, "Interpretation of dark-field contrast and particle-size selectivity in grating interferometers," *Appl. Opt.* **50**(22), 4310 (2011).

38. M. Strobl, "General solution for quantitative dark-field contrast imaging with grating interferometers," *Sci. Rep.* **4**(1), 7243 (2015).
39. Y. Sung, W. P. Segars, A. Pan, M. Ando, C. J. R. Sheppard, and R. Gupta, "Realistic wave-optics simulation of X-ray phase-contrast imaging at a human scale," *Sci. Rep.* **5**(1), 12011 (2015).
40. Y. Sung, C. J. R. Sheppard, G. Barbastathis, M. Ando, and R. Gupta, "Full-wave approach for x-ray phase imaging," *Opt. Express* **21**(15), 17547 (2013).
41. Y. Sung and G. Barbastathis, "Rytov approximation for x-ray phase imaging," *Opt. Express* **21**(3), 2674 (2013).
42. K. Willer, A. A. Fingerle, L. B. Gromann, F. De Marco, J. Herzen, K. Achterhold, B. Gleich, D. Muenzel, K. Scherer, M. Renz, B. Renger, F. Kopp, F. Kriner, F. Fischer, C. Braun, S. Auweter, K. Hellbach, M. F. Reiser, T. Schroeter, J. Mohr, A. Yaroshenko, H.-I. Maack, T. Pralow, H. van der Heijden, R. Proksa, T. Koehler, N. Wieberneit, K. Rindt, E. J. Rummeny, F. Pfeiffer, and P. B. Noël, "X-ray dark-field imaging of the human lung—A feasibility study on a deceased body," *PLoS One* **13**(9), e0204565 (2018).